scientific reports



OPEN

A general tribo-dynamic model for lubricated clearance joints in spatial multibody systems

Shuo Liu¹, Yi Cui^{1⊠}, Mingcai Xing¹, Lining Gao¹ & Feng Zhu²

Existing tribo-dynamic models encounter challenges in accurately characterizing the intense coupling and notable nonlinearity between component deformation and oil film pressure in lubricated clearance joints. Consequently, a novel general tribo-dynamic coupling model based on an absolute coordinate framework has been developed in this paper. The equations of motion for flexible multibody systems are formulated based on the absolute nodal coordinate formulation. Mixed lubrication equations are defined at spatial nodes on reference surfaces by employing the mixed Eulerian-Lagrangian approach. The model is applied to a translational clearance joint, validated through an impact test rig. Comparing the dynamical response signals from the model and experiment demonstrates its accuracy in depicting the strong coupling characteristics between deformation and pressure fields in lubricated clearance joints.

Keywords Tribo-dynamic model, Multibody systems, Mixed lubrication, Spatial and temporal discretization, Absolute coordinate frame, Lubricated clearance joints

Multibody system dynamics primarily investigate dynamic systems involving multiple joints and bodies with relative motion, offering a comprehensive abstraction and effective description of systems composed of interconnected bodies¹. In an ideal scenario, moving bodies are modeled as rigid or deformable entities, while joints are mathematically characterized through kinematic constraints. In practice, however, clearances within the joints are inevitably present due to factors such as assembly design, manufacturing errors, and wear². Clearances are critical for ensuring the proper functioning of joints, yet such clearances can also lead to system vibrations and noise, thereby reducing work efficiency. To accurately analyze or predict the dynamic characteristics of multibody systems, clearance joints are garnering increasing research attention.

Modeling of contact and friction behaviors of clearance joints can be primarily represented into two main forms. The first is the dry contact model³⁻¹⁵. In the absence of lubricant within the joints, existing clearances may induce contact-impact behaviors among the moving components. The normal contact-impact force is characterized by modified Hertz contact theory³, as exemplified by Kelvin-Voigt⁴, Hunt-Crossley⁵, and Lankarani-Nikravesh models⁶⁻⁸, among others. The tangential friction force is characterized by modified Coulomb's friction theory¹⁰. Li et al.⁶ employed a dry contact model to characterize the nonlinear contact forces of multi-planar rotating joints in a deployable solar array system. Subsequently, the impact of clearance on the dynamic characteristics and wear of the system was analyzed. Zheng et al.⁸ analyzed the motion of a flexible reciprocating slider confined between upper and lower boundaries, using the Lankarani-Nikravesh model to characterize the normal contact-impact force between the slider and boundaries. In the study of lubricated piston-liner translational joints, Guo et al.⁹ employed a dry contact model to simplify the calculation of the nonlinear contact force between the piston skirt and liners. The impact behavior and secondary motion of the piston were also investigated. Flore et al.¹⁰, however, noted that such simplifications could introduce erroneous spikes in the dynamic results.

When a fluid lubricant fills the clearance within a joint, it functions similarly to a nonlinear spring-damper element, imparting damping and stiffness to the system. This mechanism effectively dissipates unintended mechanical vibrations and prevents direct contact between moving parts, thereby attenuating friction and wear. Consequently, the second approach for simulating contact behavior at interfaces accounts for the presence of an oil film within the clearance and involves establishing a lubrication model ^{16–39}. In such a model, the normal contact force within joints is attributed primarily to the dynamic pressure and the squeezing effect of the lubricating film. The basic content of fluid lubrication analysis is the application and resolution for the Reynolds equation ¹⁷, which is a specialized form of the Navier-Stokes equation ¹⁶. Chen et al. ¹⁸ employed an analytical model for oil film

¹School of Mechanical Engineering, Shanghai Jiao Tong University, Shanghai 200240, China. ²National Key Laboratory of Marine Engine Science and Technology, Shanghai 201108, China. [⊠]email: ycui@sjtu.edu.cn

forces and explored the influence of dynamic viscosity of lubricating oil, rotational speed, and clearance on the dynamic responses of mechanisms with multiple rotating joints. However, Daniel et al.¹⁹ observed a discrepancy between the analytical oil film force model, derived using Sommerfeld or Gumbel boundary conditions, and the numerical solution of the Reynolds equation. Liu et al.^{20–22} used the finite element method (FEM) to numerically solve the Reynolds equation for lubricated translational joints in low-speed engines, focusing on how the gap between the crosshead-guide pair affects frictional loss and vibration. In parallel, Ruggiero et al.²³ utilized the finite difference method (FDM) to solve the Reynolds equation for artificial hip joints, subsequently predicting the unsteady oil film forces and material volume wear in the hip joints. In general, clearance joints in multi-body mechanical systems, whether modeled with dry contact or lubrication, can be considered as time-varying force elements rather than kinematic constraints of ideal joints.

With the evolution of applications in the automotive, maritime, robotics, medical device, and aerospace industries, research in multibody systems has increasingly extended to spatial flexible multibody systems, which account for the deformation of three-dimensional objects. In practical multibody mechanical systems subject to heavy loads, the oil film pressure within the joints can induce deformation in the moving parts. This deformation, in turn, leads to changes in the oil film pressure, thereby affecting the bearing capacity of the oil film. Dlugoš et al. 40 developed a spatial multibody system model for a high-speed vehicle engine based on the floating coordinate method^{40–43} in MSC Adams software. In the subroutine, the FDM method was utilized to solve the average Reynolds equation for the lubricant, enabling tribo-dynamic coupling modeling of piston-cylinder liner joints. To address challenges in handling large component deformations with floating coordinate methods, the absolute nodal coordinate formulation (ANCF) utilizes absolute coordinates for describing the discrete nodes of flexible bodies¹, proving effective in system modeling under large deformation conditions. This approach is regarded as a significant progress in the dynamic modeling of flexible multibody systems^{44–53}. Gantoi et al. ⁴⁵ developed a more realistic model of the knee by employing the ANCF method, where the ligaments, muscles, and soft tissues surrounding the knee joint then are modeled as flexible bodies with large deformation. Upon applying the ANCF method, the mass matrix remains constant, and the incorporation of trigonometric operations in the constraint equations and Jacobian matrix is avoided, thereby simplifying the dynamic equations of spatial flexible multibody systems substantially.

In summary, the study of tribo-dynamics, particularly concerning the coupling relationship between the three-dimensional deformation of moving components and lubrication pressure fields, represents a prominent research area in the analysis of clearance joints within multibody systems. A considerable volume of research³⁻³⁴ has investigated various types of clearance joints, including rotating, reciprocating, ball bearings, biological joints, among others. Nevertheless, some limitations remain. In spatial multibody systems, three-dimensional absolute coordinate representations are generally employed. In contrast, current lubrication models predominantly adopt a two-dimensional local coordinate representation. For the purpose of simultaneous solution, coordinates transformation is necessitated. This requirement renders the solution process for tribo-dynamics problems being sequential and interactive, posing significant challenges in accurately capturing the intense coupling effects between component deformation and lubrication pressure fields. In addition, a range of modeling methods and solution techniques exists for different clearance joints. To simplify the modeling and solving processes, it is crucial to develop a novel, general model that accurately captures the intense tribo-dynamic coupling behaviors in clearance joints within multibody systems.

Therefore, a novel, general tribo-dynamic coupling model for lubricated clearance joints in spatial flexible multibody systems is developed in this paper, utilizing an absolute coordinate framework. In Sect. 2, the equations of lubrication are then defined at spatial nodes on reference surfaces by employing the mixed Eulerian-Lagrangian approach. The motion equations for spatial flexible multibody systems are established using the ANCF method. In Sect. 3, the coupled model is discretized in space and time utilizing the FEM and a low numerical damping method. Subsequently, an integrated solving strategy is used to uniformly solve the discretized nonlinear algebraic equations. This approach ensures an accurate depiction of the strong coupling characteristics between deformation and pressure fields in lubricated clearance joints. In Sect. 4, the general model is applied to a translational clearance joint, for which an impact test rig is designed and constructed. By comparing the dynamical response signals from both the model and experiment, the versatility of the tribodynamic model and the accuracy of the integrated solution strategy are further validated.

General tribo-dynamic model for lubricated clearance joints

In this section, a general tribo-dynamic coupling model based on an absolute coordinate framework has been developed for lubricated clearance joints within spatial flexible multibody systems. By employing this model, the strong coupling characteristics between the deformation of moving parts and lubrication pressure fields can be explored.

Mixed lubrication model under absolute coordinate framework

In lubricated clearance joints, the clearance is typically much smaller than the other geometric scales. When modeling, it is not desirable to directly represent the geometric shape of lubricating film. Instead, the governing equations of thin film lubrication ought to be applied to a specific surface within the model. By employing the mixed Eulerian-Lagrangian approach^{54,55}, the equations of mixed lubrication are then defined at spatial nodes on reference surfaces, as depicted in Fig. 1.

In Fig. 1, the reference plane remains static in space. The equations governing thin film lubrication are defined at spatial nodes on these reference surfaces, allowing for the solution of fluid pressure through the Euler method. Both the wall and base are moving part surfaces, capable of relative motion with respect to the reference surface. The normal and tangential forces generated by lubrication behaviors act simultaneously on the upper and lower surfaces. Due to the oil film forces, deformation occurs in both the wall and the base. The physical properties of these deformed regions can be characterized through the Lagrangian method. In general, by employing this

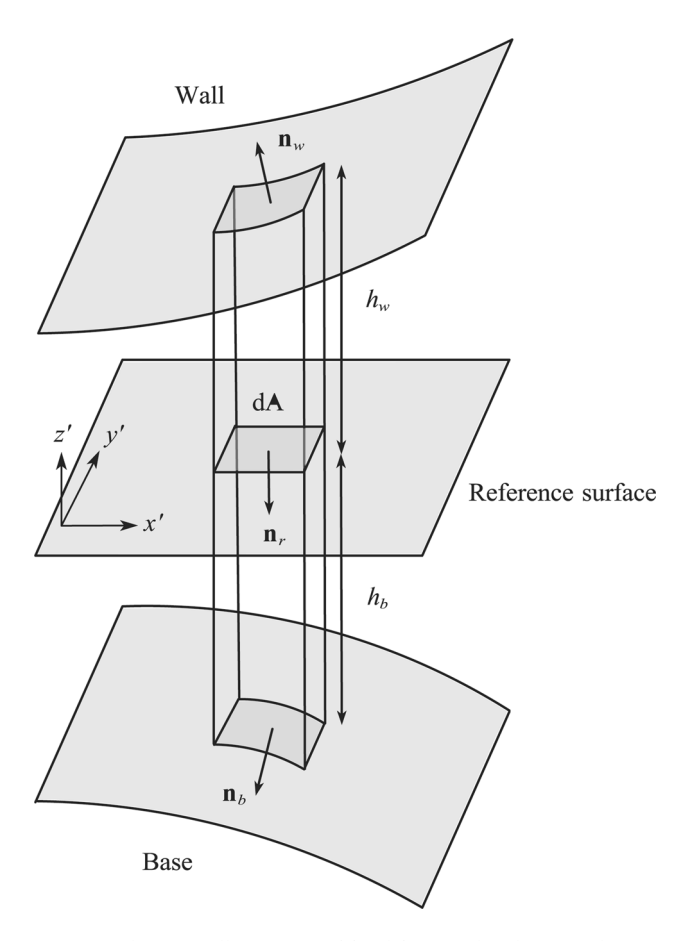


Fig. 1. Schematic illustration of fluid flow in the clearance between moving parts, with the wall and base representing the upper and lower boundaries, respectively. A reference vector, \mathbf{n}_p points from the wall towards the base. The reference plane is fixed in space, with the distances to the wall and base being h_w and h_b , respectively. A finite control volume is attached to the reference plane, with a height h varying depending on the positions of the wall and base. The outward normal vectors on the surfaces of this control volume are \mathbf{n}_w and \mathbf{n}_b , respectively. The projected area on the reference plane is denoted as dA.

mixed Eulerian-Lagrangian approach, the need to represent the geometric shape of lubricating film is eliminated, and the governing equations of lubrication model can be directly defined on the reference surface.

Considering the working conditions of lubricated clearance joints, moving parts may pass through mixed lubrication zones. Building on existing research on the average Reynolds Eqs^{56–58} and applying the continuity equation to the finite control volume depicted in Fig. 1, the control equation for mixed lubrication within an absolute coordinate framework can be derived as,

$$\nabla \cdot (\rho h \bar{\mathbf{v}}_{av}) + \phi_c \frac{\partial (\rho h)}{\partial t} = 0, \tag{1}$$

where ∇ denotes the Nabla operator. $\bar{\mathbf{v}}_{av}$ is the average flow velocity on the reference surface. ϕ_c represents the contact factor. ρ is the density. h represents the height of the finite control volume, defined at spatial nodes on the reference surface. As h varies with the positions of the wall and the base, it can be expressed as,

$$h = h_w + h_b. (2)$$

In Eq. (2), h_w and h_b represent the distances from reference face to the wall and base, respectively. The flow velocity of the lubricant film along its thickness is affected by both Couette and Poiseuille flows. $\bar{\mathbf{v}}_{av}$ can then be formulated as,

$$\bar{\mathbf{v}}_{av} = \underbrace{\frac{1}{2}\phi_c \left(\mathbf{I} - \mathbf{n}_r \mathbf{n}_r^{\mathrm{T}}\right) \left(\mathbf{v}_w + \mathbf{v}_b\right) + \frac{1}{2}\phi_s \frac{\sigma}{h} \left(\mathbf{I} - \mathbf{n}_r \mathbf{n}_r^{\mathrm{T}}\right) \left(\mathbf{v}_w - \mathbf{v}_b\right)}_{Couette\ flow} - \underbrace{\frac{h^2}{12\mu} \nabla p}_{Poiseuille\ flow}, \tag{3}$$

Where p is the oil film pressure to be solved. \mathbf{v}_{w} and \mathbf{v}_{b} represent the oil film flow velocities over the wall and base, respectively. σ represents the combined roughness of upper and lower surfaces. \mathbf{n}_{c} is the normal vector of

the reference surface. ϕ_i and ϕ_s correspond to the pressure flow factor and the shear flow factor, respectively, which characterize the influence of the rough surface on the fluid film flow. By combining Eqs. (1), (2), and (3), a mixed lubrication model is established for lubricated clearance joints within an absolute coordinate framework. Except in certain oil-starved conditions, the boundary oil film pressure can be set to ambient pressure. Upon imposing appropriate boundary conditions, the oil film pressure at each spatial node on the reference surface can be solved.

Asperities contact and forces transmitted to moving parts

In the mixed lubrication model, the forces exerted on moving part surfaces mainly include pressure and friction. During the state of mixed lubrication in a clearance joint, asperities contact often occurs on the surfaces. Consequently, pressure comprises both oil film pressure p and asperity contact pressure p_c , together supporting normal loads and causing vibration and deformation of moving parts. Frictional forces comprise oil film shear stress τ and asperity shear stress τ_c , constituting a significant component of frictional losses in mechanical systems.

Based on the work of Greenwood and Tripp⁵⁹, the asperity contact pressure p_c is characterized as,

$$p_c(h) = KE' F_{5/2}(H_\sigma).$$
 (4)

The G/T model posits that the distribution of asperities conforms to a Gaussian distribution. The heights of asperities (micro-contact peaks) on the surface follow a statistical distribution, such as a normal distribution. At each asperity, the local deformation upon contact adheres to Hertzian contact theory, where only the normal load is considered. The contact pressure exerted by these asperities is determined using Hertzian contact theory. In Eq. (4), K represents the elastic coefficient, with the value ranging from 0.0003 to 0.003. E' is the comprehensive elastic modulus. H_{σ} is the film thickness ratio. $F_{5/2}(H_{\sigma})$ represents probability distribution of asperity heights. Asperity shear stress τ_c is calculated as the product of friction coefficient μ_f and contact pressure p_c :

$$\tau_c = \mu_f p_c. \tag{5}$$

Under mixed lubrication conditions, velocity variation across the oil film thickness is extensive. The shear stress in the oil film, denoted as τ , is primarily determined by the velocity gradient in this direction. According to relevant studies on the average Reynolds Eqs^{56–58}, the oil film shear stress τ is obtained as,

$$\begin{cases}
\tau_{z'x'} = \frac{\mu}{h} \left(v_{x'}^{w} - v_{x'}^{b} \right) \left(\phi_{f} \pm \phi_{fs} \right) + \frac{\phi_{fp}}{2} \frac{\partial p}{\partial x'} \left(2z' - h_{w} + h_{b} \right), \\
\tau_{z'y'} = \frac{\mu}{h} \left(v_{y'}^{w} - v_{y'}^{b} \right) \left(\phi_{f} \pm \phi_{fs} \right) + \frac{\phi_{fp}}{2} \frac{\partial p}{\partial y'} \left(2z' - h_{w} + h_{b} \right).
\end{cases} (6)$$

In Eq. (6), the left and right terms represent the shear stresses caused by Couette and Poiseuille flows, respectively. The local coordinate system within the lubrication domain is denoted by x', y', and z', where z' corresponds to the direction of thickness, as illustrated in Fig. 1. $v_{x'}$ and $v_{y'}$ are the flow velocities in the directions of x' and y', respectively. ϕ_p , ϕ_{fs} , and ϕ_{fp} represent shear stress factors ^{56–58}. Considering oil film pressure p, asperity contact pressure p_c , oil film shear stress τ , and asperity shear stress τ_c , the forces \mathbf{f}_w and \mathbf{f}_b on the upper and lower surfaces in the mixed lubrication model can be formulated in vector form within an absolute coordinate framework as,

$$\begin{cases}
\mathbf{f}_{w} = \mathbf{f}_{w,\tau} + \mathbf{f}_{w,\tau c} + \mathbf{f}_{w,p} + \mathbf{f}_{w,pc}, \\
\mathbf{f}_{b} = \mathbf{f}_{b,\tau} + \mathbf{f}_{b,\tau c} + \mathbf{f}_{b,p} + \mathbf{f}_{b,pc},
\end{cases} (7)$$

where

$$\begin{cases}
\mathbf{f}_{w,\tau} = \frac{\mu}{h} \left(\phi_f + \phi_{fs} \right) \left(\mathbf{I} - \mathbf{n}_r \mathbf{n}_r^{\mathrm{T}} \right) \left(\mathbf{v}^b - \mathbf{v}^w \right) - \phi_{fp} \frac{h}{2} \nabla_{\tau} p, \\
\mathbf{f}_{b,\tau} = \frac{\mu}{h} \left(\phi_f - \phi_{fs} \right) \left(\mathbf{I} - \mathbf{n}_r \mathbf{n}_r^{\mathrm{T}} \right) \left(\mathbf{v}^w - \mathbf{v}^b \right) - \phi_{fp} \frac{h}{2} \nabla_{\tau} p, \\
\mathbf{f}_{w,\tau c} = \frac{\left(\mathbf{I} - \mathbf{n}_r \mathbf{n}_r^{\mathrm{T}} \right) \left(\mathbf{v}^b - \mathbf{v}^w \right)}{\left| \left(\mathbf{I} - \mathbf{n}_r \mathbf{n}_r^{\mathrm{T}} \right) \left(\mathbf{v}^b - \mathbf{v}^w \right) \right|} \mu_f p_c, \\
\mathbf{f}_{b,\tau c} = \frac{\left(\mathbf{I} - \mathbf{n}_r \mathbf{n}_r^{\mathrm{T}} \right) \left(\mathbf{v}^w - \mathbf{v}^b \right)}{\left| \left(\mathbf{I} - \mathbf{n}_r \mathbf{n}_r^{\mathrm{T}} \right) \left(\mathbf{v}^w - \mathbf{v}^b \right) \right|} \mu_f p_c, \\
\mathbf{f}_{w,p} = p \mathbf{n}_w, \\
\mathbf{f}_{b,p} = p \mathbf{n}_b, \\
\mathbf{f}_{w,pc} = p_c \mathbf{n}_w, \\
\mathbf{f}_{b,pc} = p_c \mathbf{n}_b.
\end{cases} \tag{8}$$

Dynamic model of spatial flexible multibody systems

The motion and deformation of spatial flexible multibody systems are characterized using the absolute nodal coordinate formulation (ANCF)^{1,44–53} in this section. The discrete nodes of flexible bodies are described by absolute coordinates. The physical properties of deformable solids, including stress, strain, and deformation, are

characterized through a complete Lagrangian format and defined on the reference configuration at the initial moment. First, the dynamic equations for each component of spatial multibody systems are established, and can be expressed as,

$$\rho \frac{\partial^2 \mathbf{u}}{\partial t^2} = \nabla_X \cdot \mathbf{P}^{\mathrm{T}} + \mathbf{F}_V, \tag{9}$$

where **P** represents the first Piola-Kirchhoff stress, defined in the initial reference configuration. ∇_X denotes the Nabla operator relative to the material framework X. \mathbf{F}_V represents the volume force vector. \mathbf{u} is the displacement vector. $\boldsymbol{\rho}$ is the material density. The stress boundary conditions can be expressed as,

$$\mathbf{P} \cdot \mathbf{n}_0 = \mathbf{F}_A. \tag{10}$$

In the formula, \mathbf{n}_0 denotes the normal vector of undeformed surface. \mathbf{F}_A represents the boundary load vector. According to the energy conjugate relationship between stress and strain 60,61, the equivalent integral weak form of dynamic Eq. (9) and stress boundary conditions (10) can be expressed as,

$$\int_{V} \left[-\delta \mathbf{E} : \mathbf{S} + \delta \mathbf{u} \cdot \mathbf{F}_{V} - \rho \delta \mathbf{u} \cdot \frac{\partial^{2} \mathbf{u}}{\partial t^{2}} \right] dV + \int_{S} \delta \mathbf{u} \cdot \mathbf{F}_{A} dS = 0, \tag{11}$$

where $\delta \mathbf{u}$ represents the virtual displacement. \mathbf{S} represents the second Piola-Kirchhoff stress tensor. \mathbf{E} denotes the Green-Lagrange strain tensor. Based on the nonlinear FEM and ANCF method, the displacement field \mathbf{u} can be discretized into the generalized nodal displacement in absolute coordinates. The dynamic equations for each body in the multi-body system can be derived as,

$$M\ddot{\mathbf{q}} + C\dot{\mathbf{q}} + \mathbf{K}\mathbf{q} = \mathbf{Q}.\tag{12}$$

In Eq. (12), \mathbf{q} represents the nodal generalized coordinate vector. \mathbf{C} denotes the Rayleigh damping. The expression of these coefficient matrices can be found in references^{60,61}. \mathbf{Q} represents the external force vector. In typical multibody systems, the components are primarily interconnected through various ideal joints. These joints are mathematically defined by kinematic constraints, which can be described as,

$$\mathbf{\Phi}\left(\mathbf{q},t\right) = \mathbf{0},\tag{13}$$

where Φ represents the constraint vector. The constraint equations for various ideal joints, as formulated using the ANCF method, are detailed in references^{45–47}. By integrating the motion equations of each component (12) and the constraint equations of each motion pair (13), the motion equations for multi-body systems can ultimately be formulated as,

$$\begin{cases} \mathbf{M}\ddot{\mathbf{q}} + \mathbf{C}\dot{\mathbf{q}} + \mathbf{K}\mathbf{q} + \mathbf{\Phi}_{\mathbf{q}}^{\mathrm{T}}(\mathbf{q}) \lambda = \mathbf{Q}, \\ \mathbf{\Phi}(\mathbf{q}, t) = \mathbf{0}. \end{cases}$$
(14)

In Eq. (14), λ represents the Lagrangian multiplier vector. $\Phi_{\mathbf{q}} = \partial \Phi/\partial \mathbf{q}$ denotes the Jacobian matrix. Different from the floating coordinate method used in previous studies, the ANCF method applied in this paper directly formulates the motion equations for spatial flexible multibody systems using absolute coordinates of spatial nodes. As the conversion between absolute and floating coordinates is unnecessary, the mass matrix remains constant. Furthermore, the incorporation of trigonometric operations in the constraint equations and Jacobian matrix is avoided, thereby simplifying the equations of motion substantially. Unlike ideal joints, clearance joints can be considered as time-varying force elements. In multibody systems, the mixed lubrication model affects by applying generalized forces to the surfaces of interconnected moving parts, rather than imposing kinematic constraints as in ideal joints.

Solution procedure for the tribo-dynamic model

This section discretizes the coupled model's control equations through a unified approach for both spatial and temporal domains, using the FEM and generalized- α method. By integrating and solving the discretized nonlinear algebraic equations within one time step, the solution strategy ensures an accurate depiction of the strong coupling characteristics between deformation and pressure fields in lubricated clearance joints.

Spatial discretization

The control Eq. (1) for mixed lubrication is spatially discretized employing the standard FEM method $^{61-66}$. In comparison to the traditional FDM method $^{67-70}$, the FEM method is better suited for irregular boundaries and ensures both convergence and computational efficiency. Based on the Green theorem, the equivalent integral weak form of Eq. (1) is obtained as,

$$\int_{\Omega} \left[(\rho h \bar{\mathbf{v}}_{av}) \cdot \nabla \delta p \right] d\Omega - \int_{\Omega} \left[\phi_c \frac{\partial (\rho h)}{\partial t} \delta p \right] d\Omega = 0.$$
 (15)

To accurately determine pressure distribution across the entire lubrication area, it is necessary to subdivide the lubrication domain into either triangular or quadrilateral grids. Within an internal element Ω^e , the pressure p can be expressed as,

$$p = \mathbf{N}^{\mathrm{T}} \mathbf{p}^{e}. \tag{16}$$

In the formula, **P** denotes the nodal pressure. **N** represents the shape function. In the numerical examples later in this paper, the lubrication domain is discretized into quadrilateral grids. The shape functions are defined as,

$$N_i(\xi, \eta) = \frac{1}{4} (1 + \xi \xi_i) (1 + \eta \eta_i), \quad i = 1, 2, 3, 4,$$
(17)

where ξ and η are the natural coordinates in the parametric space, while ξ_i and η_i denote the local coordinates of node *i*. Combining Eq. (16) with Eq. (15) and taking into account the arbitrariness of $\delta \mathbf{p}^e$, the algebraic equations for determining the pressure within the element Ω^e are expressed as,

$$\mathbf{K}^e \mathbf{p}^e = \mathbf{F}^e. \tag{18}$$

In Eq. (18), K^e and F^e denote the element stiffness matrix and nodal load vector, respectively, represented as,

$$\begin{cases}
\mathbf{K}^{e} = -\int_{\Omega^{e}} \phi_{i} \frac{\rho h^{3}}{12\mu} \left[\left(\nabla \mathbf{N}^{T} \right)^{T} \nabla \mathbf{N}^{T} \right] d\Omega, \\
\mathbf{F}^{e} = \int_{\Omega^{e}} \left\{ \rho h \left(\nabla \mathbf{N}^{T} \right)^{T} \left[\frac{1}{2} \phi_{c} \left(\mathbf{I} - \mathbf{n}_{r} \mathbf{n}_{r}^{T} \right) \left(\mathbf{v}_{w} + \mathbf{v}_{b} \right) \right. \\
+ \frac{1}{2} \phi_{s} \frac{\sigma}{h} \left(\mathbf{I} - \mathbf{n}_{r} \mathbf{n}_{r}^{T} \right) \left(\mathbf{v}_{w} - \mathbf{v}_{b} \right) \right] - \phi_{c} \frac{\partial \left(\rho h \right)}{\partial t} \mathbf{N} \right\} d\Omega.
\end{cases} \tag{19}$$

In the formula, the derivatives with respect to the global coordinates x, y, and z, are calculated using the chain rule. The derivatives in the natural coordinate system are expressed as,

$$\frac{\partial N_i}{\partial \xi} = \frac{1}{4} \eta_i \left(1 + \eta \eta_i \right), \quad \frac{\partial N_i}{\partial \eta} = \frac{1}{4} \xi_i \left(1 + \xi \xi_i \right). \tag{20}$$

The derivatives with respect to the global coordinates are obtained via the Jacobian matrix *J*, which relates the natural coordinates to the global coordinates:

$$\left\{ \begin{array}{l} \frac{\partial N_i}{\partial \mathcal{R}_i} \\ \frac{\partial N_i}{\partial y} \\ \frac{\partial N_i}{\partial z} \end{array} \right\} = J^{\mathrm{T}} \left(J J^{\mathrm{T}} \right)^{-1} \left\{ \begin{array}{l} \frac{\partial N_i}{\partial \xi} \\ \frac{\partial N_i}{\partial \eta} \end{array} \right\}, \ J = \left(\begin{array}{ccc} \frac{\partial x}{\partial \xi} & \frac{\partial y}{\partial \xi} & \frac{\partial z}{\partial \xi} \\ \frac{\partial x}{\partial \eta} & \frac{\partial y}{\partial \eta} & \frac{\partial z}{\partial \eta} \end{array} \right). \tag{21}$$

By assembling Eq. (18), a set of nonlinear algebraic equations within domain Ω would be fully determined.

Temporal discretization

The differential-algebraic equations (DAEs) for three-dimensional multibody systems, as shown in Eq. (14), requires further conversion into nonlinear algebraic equations through temporal discretization methods before solving. Common methods include the BDF method^{71–73}, Newmark- β method^{74–76}, HHT method⁷⁷, and the generalized- α method^{78–83}. For the computational results expected in this study, which include solutions with steep gradients such as vibration signals, the chosen temporal discretization algorithm should exhibit characteristics of low numerical damping.

Among these methods, the generalized- α method^{78–83} is a second-order implicit method, incorporating a parameter α to control the numerical damping. For the DAEs as presented in Eq. (14), the generalized- α method can be expressed as,

$$\begin{cases}
\mathbf{M}\ddot{\mathbf{q}}_{n+1-\alpha_m} + \mathbf{C}\dot{\mathbf{q}}_{n+1-\alpha_f} + \mathbf{K}\mathbf{q}_{n+1-\alpha_f} + \mathbf{\Phi}_{\mathbf{q}}^{\mathrm{T}} \left(\mathbf{q}_{n+1-\alpha_f} \right) \lambda_{n+1} = \mathbf{Q} \left(t_{n+1-\alpha_f} \right), \\
\mathbf{\Phi} \left(\mathbf{q}_{n+1}, t_{n+1} \right) = 0,
\end{cases}$$
(22)

Where semi-discrete quantities can be expressed as,

$$\begin{cases}
\ddot{\mathbf{q}}_{n+1-\alpha_m} = (1 - \alpha_m) \ddot{\mathbf{q}}_{n+1} + \alpha_m \ddot{\mathbf{q}}_n, \\
\dot{\mathbf{q}}_{n+1-\alpha_f} = (1 - \alpha_f) \dot{\mathbf{q}}_{n+1} + \alpha_f \dot{\mathbf{q}}_n, \\
\mathbf{q}_{n+1-\alpha_f} = (1 - \alpha_f) \mathbf{q}_{n+1} + \alpha_f \mathbf{q}_n, \\
t_{n+1-\alpha_f} = (1 - \alpha_f) t_{n+1} + \alpha_f t_n.
\end{cases} (23)$$

The predicted values at time step n+1 can be calculated as,

$$\begin{cases}
\ddot{\mathbf{q}}_{n+1} = \frac{1}{\beta \Delta t^2} \left(\mathbf{q}_{n+1} - \mathbf{q}_n \right) - \frac{1}{\beta \Delta t} \dot{\mathbf{q}}_n - \left(\frac{1}{2\beta} - 1 \right) \ddot{\mathbf{q}}_n, \\
\dot{\mathbf{q}}_{n+1} = \frac{\gamma}{\beta \Delta t} \left(\mathbf{q}_{n+1} - \mathbf{q}_n \right) - \left(\frac{\gamma}{\beta} - 1 \right) \dot{\mathbf{q}}_n - \Delta t \left(\frac{\gamma}{2\beta} - 1 \right) \ddot{\mathbf{q}}_n.
\end{cases} (24)$$

The motion equations for multi-body systems, presented in Eq. (14), can be temporally discretized into nonlinear algebraic equations in Eqs. (22), (23), and (24). The generalized- α method ensures second-order accuracy⁷⁸, with parameters selected as,

$$\begin{cases}
\alpha_m = \frac{2\rho_{\infty} - 1}{\rho_{\infty} + 1}, \ \alpha_f = \frac{\rho_{\infty}}{\rho_{\infty} + 1}, \quad \rho_{\infty} \in [0, 1], \\
\beta = \frac{1}{4} (1 - \alpha_m + \alpha_f)^2, \ \gamma = \frac{1}{2} - \alpha_m + \alpha_f.
\end{cases}$$
(25)

In the formula, ρ_{∞} represents the numerical dissipation, with the dissipation decreasing as the value approaches 1. When both α_m and α_f are equal to 0, the generalized- α method degenerates into the Newmark- β method. The temporal discretization based on the generalized- α method offers low numerical damping, allowing for accurate dynamic response calculations.

Integrated solving strategy for the coupled model

The tribo-dynamic coupling model proposed in this paper uses a unified absolute coordinate framework, enabling simultaneous solutions for mixed lubrication and spatial multibody dynamics without requiring coordinate transformation. Therefore, an integrated numerical solution strategy is adopted for the coupled model. By integrating and solving the discretized nonlinear algebraic equations within one time step, this strategy ensures an accurate depiction of the strong coupling characteristics between deformation and pressure fields in lubricated clearance joints. Through progressive time-stepping, the calculation results for the unknown variables can be yielded at each time step.

Combining Eqs. (18)-(24), the nonlinear algebraic equations for unknown physical fields such as displacement and pressure in lubricated clearance joints can be integrated and expressed as,

$$\mathbf{f} = \begin{pmatrix} \mathbf{K}_{p} (\mathbf{u}_{\mathbf{q}}) & 0 \\ 0 & \mathbf{K}_{\mathbf{q}} (\mathbf{u}_{\mathbf{q}}) \end{pmatrix} \begin{pmatrix} \mathbf{u}_{p} \\ \mathbf{u}_{\mathbf{q}} \end{pmatrix} - \begin{pmatrix} \mathbf{b}_{p} (\mathbf{u}_{\mathbf{q}}) \\ \mathbf{b}_{\mathbf{q}} (\mathbf{u}_{p}) \end{pmatrix}, \tag{26}$$

where the unknown physical field variables are uniformly denoted by \mathbf{u}_p and \mathbf{u}_q . The subscripts p and \mathbf{q} represent pressure and generalized displacement, respectively. In Eq. (26), the strong coupling characteristics between the deformation of moving components and the pressure in mixed lubrication is effectively integrated. The terms \mathbf{K} and \mathbf{b} symbolize the coefficient matrices and load terms, encapsulating the interactions between the two fields.

In one time step, the nonlinear algebraic equations of the tribo-dynamic coupled model, as depicted in Eq. (26), are iteratively solved utilizing the Newton-Raphson method. As time progresses, the oil film pressure and dynamic responses of multibody systems can be solved for the entire duration. The detailed solution procedure for the coupled model is illustrated in Fig. 2.

Experimental verification of the general tribo-dynamic model

This section applies the proposed general tribo-dynamic model to a translational clearance joint with reciprocating motion, for which an impact test rig is designed and constructed. By comparing the dynamical response signals obtained from both the model and the experiment under dry contact and lubrication conditions, the versatility of the tribo-dynamic model and the accuracy of the integrated solution strategy has been validated.

Impact test rig for translational clearance joint

In the impact test rig to be constructed, a slider and a guide constitute a basic translational clearance joint. The guide is fixed at both ends to a rigid base using bolts. The slider, operating under various lubrication conditions, is driven by a motor, enabling it to reciprocate along the guide. An impact hammer delivers the impact load to the slider at specific locations, exciting vibrations in both the slider and the guide. The design schematic of the impact test rig is shown in Fig. 3. To validate the accuracy of the general tribo-dynamic model, dynamical response signals from both the model and the experiment are compared under the same impact load from the hammer, encompassing conditions of dry contact and lubrication.

In a similitude treatment for a crosshead-guides translational joint in low-speed marine engines, dimensional parameters of the slider and guide used in the test rig are determined and presented in Table 1. More specifically, the dimensions of the slider are determined by the similarity in lubrication states, characterized by the pressure ratio. Furthermore, the dimensions of the guide are determined by their similarity in first-order natural frequency.

As shown in Fig. 3, a guide rod, supported by a linear bearing, is connected to the slider through a double hinge joint. This configuration ensures that the slider is subjected only to the lateral impact load applied by the hammer, minimizing the influence of the driving mechanism on the vibration measurement of both the slider and guide. Force and acceleration sensors are assembled to measure the impact load of the hammer and vibration signals of the slider and the guide, respectively. To satisfy the requirements for high-frequency output, piezoelectric sensors that generate Integrated Electronics Piezo-Electric (IEPE) voltage signals were employed in

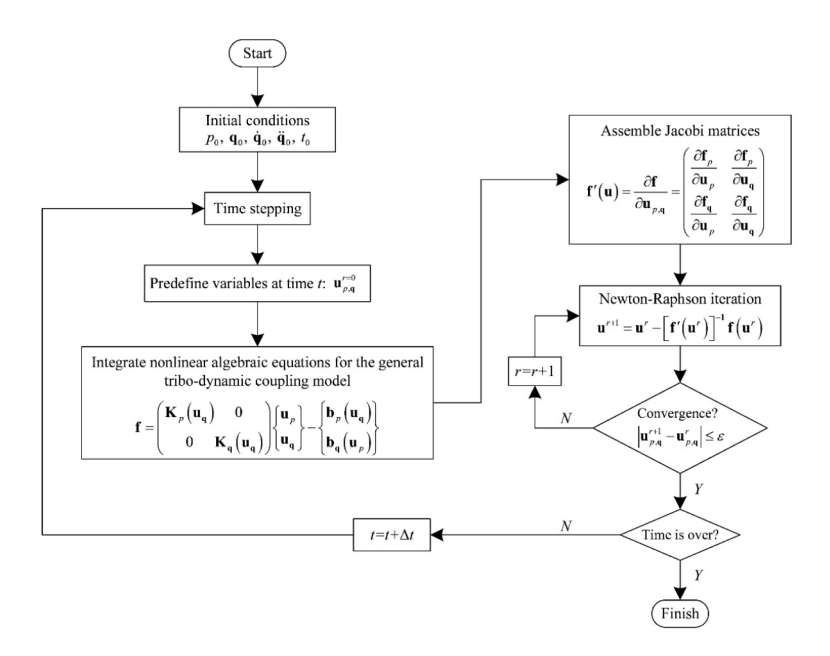


Fig. 2. Workflow for solving the tribo-dynamic coupling model. Through time stepping, unknown physical fields are determinable for the entire simulation period.

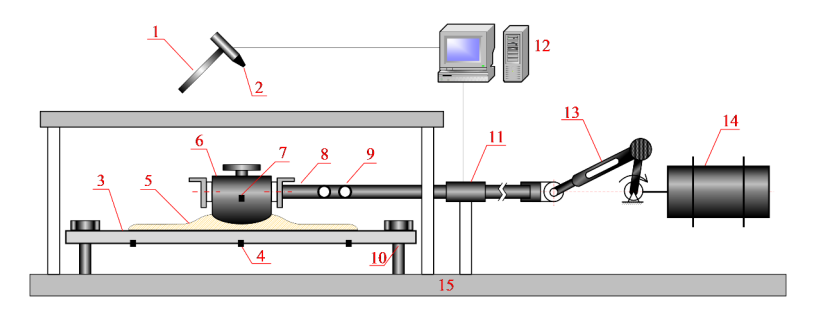


Fig. 3. Design schematic of an impact test rig for a translational clearance joint with reciprocating motion: (1) impact hammer; (2) hammer head with an integrated piezoelectric force sensor; (3) guide; (4) acceleration sensors; (5) lubricating medium; (6) slider; (7) three-way acceleration sensor; (8) guide rod; (9) hinge joints; (10) bolts; (11) linear bearings; (12) digital signal acquisition and control system; (13) connecting rod; (14) drive motor; (15) rigid foundation.

Parameters	Descriptions	Values
L_r	Length of slider	40 (mm)
W_r	Width of slider	40 (mm)
H_r	Height of slider	30 (mm)
L_{g}	Length of guide	340 (mm)
W_{g}	Width of guide	50 (mm)
H_{α}	Height of guide	5 (mm)

Table 1. Dimensional parameters of the slider and the guide used in the impact test rig.

the experiment. These sensors mainly include a force sensor below the hammer head, a three-way acceleration sensor on the slider, and uniformly distributed acceleration sensors under the guide. Dynamic signals of the test rig are collected in real-time by the DH8303 dynamic signal acquisition system. The measurement and control system, consisting of 32 signal channels and capable of a maximum signal acquisition frequency of 256 kHz, satisfies the experimental requirements. Finally, the impact test rig for experimental research is shown in Fig. 4.

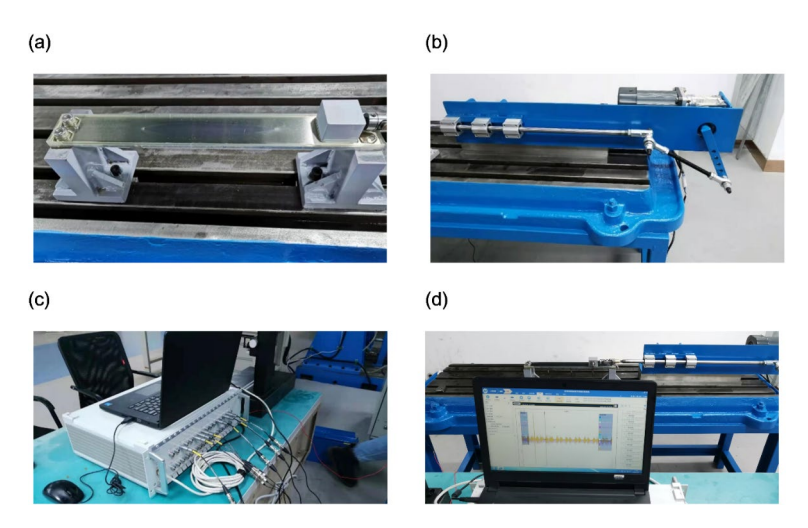


Fig. 4. Impact test rig for experimental research: (a) slider-guide translational joint; (b) drive mechanism; (c) signal acquisition system; (d) layout of bench and acquisition system.

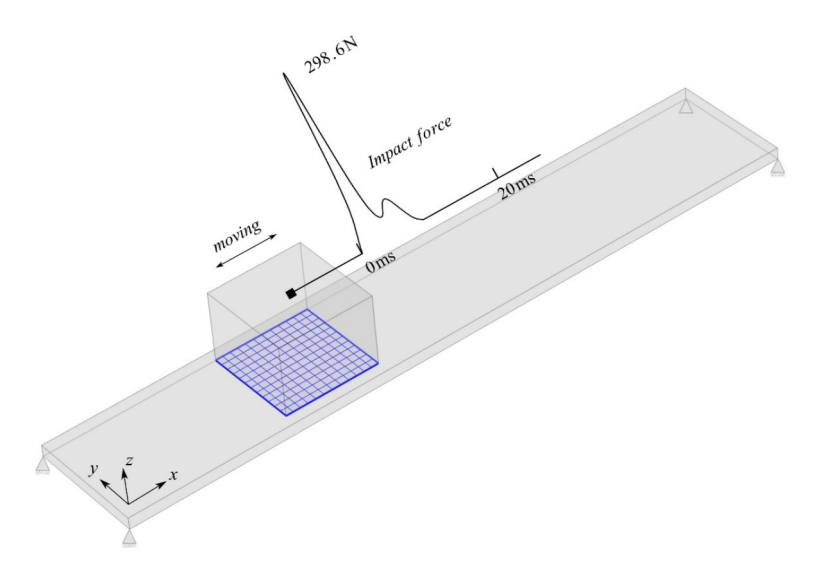


Fig. 5. Schematic diagram of the tribo-dynamic model for the translational clearance joint. The model fundamentally aligns with the experimental setup. The slider reciprocates along the guide, with both components treated as three-dimensional flexible bodies. The lubrication domain is divided into these quadrilateral grids, where *xyz* represent absolute coordinates. The measured impact load of the hammer is applied within 10 ms, reaching a maximum of 298.6 N.

Tribo-dynamic model for translational clearance joint

A tribo-dynamic model for the translational clearance joint, which fundamentally aligns with the experimental setup, has been established by applying the previously proposed general tribo-dynamic model. The schematic diagram of the model is illustrated in Fig. 5. In the figure, the slider reciprocates along the guide. Both components are treated as three-dimensional flexible bodies. The motion equations of the system are presented in Eq. (14). Constraints on the slider and the guide, such as the fixed constraint of the guide and the motion speed of the slider, are reflected in the constraint vector Φ . The force vector \mathbf{Q} includes the measured impact load from the hammer and forces from mixed lubrication, such as pressure and friction forces. The measured impact load of the hammer, as depicted in Fig. 5, is applied within 10 ms and recorded at a sampling frequency of 20 kHz.

The lubrication behaviors of the translational joint are characterized by Eq. (1), which is defined at spatial nodes using the Euler method, as depicted in Fig. 5. Both the boundary pressure and the initial pressure are set equal to the ambient pressure. The film thickness h is described as,

$$h = h_0 + h_{prof} + h_s + d_r + d_g, (27)$$

where h_0 is the initial oil film thickness. h_{prof} represents the profile at the bottom of slider. h_s denotes the film thickness variation induced by the secondary motion external to the reciprocating movement of the slider. d_r

and d_g correspond to the film thickness variations arising from elastic deformations of the slider and guide, respectively. Correspondingly, the physical properties of both the slider and the guide can be described using the Lagrangian method.

In addition, a dry contact model for the translational joint is introduced in this section, as a substitute for the lubrication model. This modification aims to facilitate a comparative analysis of the vibration responses in the joint, both in the presence and absence of an oil film. Such a comparison further substantiates the universality and precision of the coupled model proposed in this study. The normal contact force, included in the force vector \mathbf{Q} , is characterized using the Lankarani-Nikravesh dry contact model^{6–8} and is defined as,

$$F_N = K_g \delta^n + \eta \delta^n \dot{\delta},\tag{28}$$

where the normal contact force consists of both elastic and damping forces. δ represents the generalized penetration depth. K_g and η are the generalized stiffness coefficient and viscous damping factor, respectively. There expressions are available in reference. The index n for metal contact is typically set to 1.5. The main input data of the coupled model for the translational clearance joint is presented in Table 2.

Comparison between model and experiment

Before applying the impact load, sliders in both the model and the experiment exhibited a stable state of reciprocating motion. The points selected for extracting vibration signals in the model correspond to the locations of vibration sensors on the impact test rig, as depicted in Fig. 3. Additionally, the calculation frequency for vibration signals in the model is set to 20 kHz, matching the experimental sampling frequency. Under dry contact conditions without oil film, the comparison of vibration signals between the model and the experiment is illustrated in Fig. 6.

In Fig. 6, the vibration acceleration signals of components from both the model and the experiment exhibit good alignment within the initial 30 ms. The vibration amplitudes of both components approximate to 400 m/s². Beyond 30 ms, however, notable discrepancies are observed in the vibrational acceleration signals obtained from the model and the experiment. The dry contact model employed in this study evidently falls short in fully representing the high-frequency and high-amplitude vibration responses observed in the experiment. However, the goal of demonstrating the general model's adaptability across various conditions is achieved, even if some details are less precise under dry contact conditions.

Under oil film lubrication conditions, the comparison of vibration signals for the general model, conventional model⁴⁰⁻⁴³, and experimental data is shown in Fig. 7. It is noteworthy that the oil film pressure beneath the slider can be calculated at any given moment. The pressure distribution of oil film at 28 ms is illustrated in Fig. 8.

In Fig. 7, the vibration acceleration signals from the general model, conventional model, and experimental data under lubrication conditions are compared, demonstrating a high degree of agreement throughout the entire response duration. The amplitude and frequency of the vibration signals depicted in Fig. 7 are nearly identical, thereby validating the versatility of the proposed tribo-dynamic model for lubricated clearance joints and the accuracy of the integrated solution strategy. The conventional model exhibits higher computational damping, leading to slightly larger errors. While the precision of both models is acceptable, the most notable advantage of the general model lies in its universality.

As emphasized in the Introduction, conventional methods for systems such as rotational joints and ball-bearing are often inconsistent and rely heavily on specific local formulations. In contrast, the proposed general model offers a unified framework that simplifies the modeling process and enhances its applicability across diverse systems.

Parameters	Descriptions	Values
μ	Viscosity of lubricating oil	0.045 (Pa·s)
ρ	Density of lubricating oil	889 (kg/m³)
h_0	Initial oil film thickness	40 (um)
p_0	Ambient pressure	1.013e5 (Pa)
λ	Connecting rod ratio	0.64
n	Rotate speed of drive motor	60 (r/min)
m_r	Mass of slider	0.374 (kg)
m_{g}	Mass of guide	0.663 (kg)
ρ_s	Density of components	7800 (kg/m ³)
E	Elastic modulus of components	210e9 (Pa)
ν	Poisson's ratio of components	0.30
K_{g}	Generalized stiffness coefficient	70e6 (N/m ^{1.5})
η	Viscous damping factor	50e7 (N·s/m ^{2.5})

Table 2. Input data of the tribo-dynamic model for the translational clearance joint.

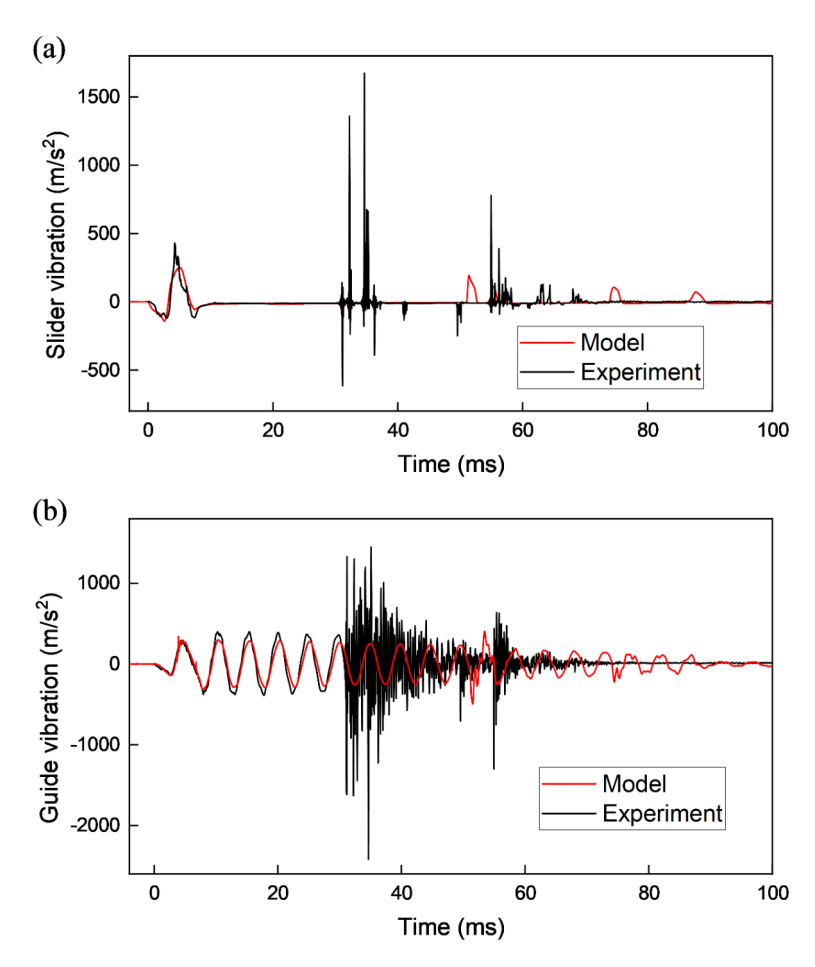


Fig. 6. Comparison of results between model and experiment under dry contact conditions: (a) vibration acceleration signals of the slider; (b) vibration acceleration signals at the middle position of the guide.

Conclusions

In this paper, a novel, general tribo-dynamic coupling model for lubricated clearance joints in spatial flexible multibody systems has been developed, utilizing an absolute coordinate framework. In the model, mixed lubrication equations are defined at spatial nodes on reference surfaces by employing the mixed Eulerian-Lagrangian approach. The equations of motion for flexible multibody systems are formulated based on the absolute nodal coordinate formulation.

The coupled model uses a unified absolute coordinate framework, enabling simultaneous solutions for mixed lubrication and spatial multibody dynamics without requiring coordinate transformation. In solving the coupled model, the control equations are discretized through a unified approach for both spatial and temporal domains, using the FEM and generalized- α method. By integrating and solving the discretized nonlinear algebraic equations within one time step, the solution strategy ensures an accurate depiction of the strong coupling characteristics between deformation and pressure fields in lubricated clearance joints.

Finally, the general model is applied to a translational clearance joint, for which an impact test rig is designed and constructed. A comparative analysis of dynamical response signals from both the model and experiment under dry contact and lubrication conditions is conducted. The goal of demonstrating the general model's adaptability across various conditions is achieved, even if some details are less precise under dry contact conditions. Under lubrication conditions, the vibration acceleration signals from both the models and the experimental setup demonstrate a high degree of agreement throughout the entire response duration. The conventional model exhibits higher computational damping, leading to slightly larger errors. While the precision of both models is acceptable, the most notable advantage of the general model lies in its universality.

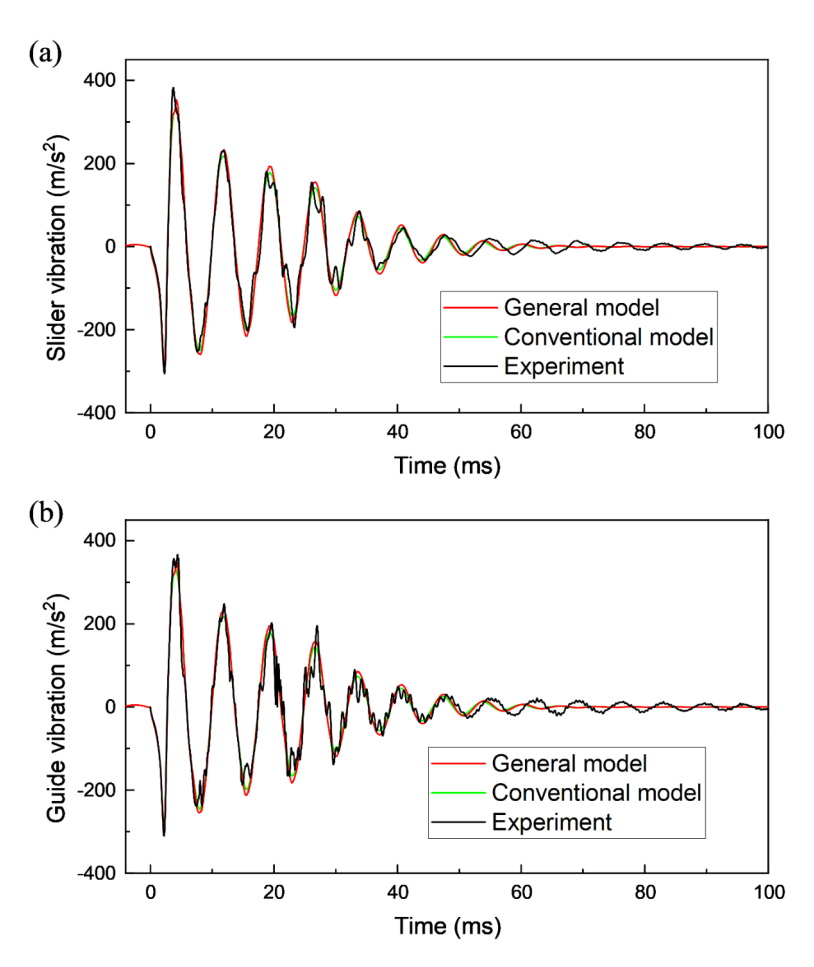


Fig. 7. Comparison of results for the general model, conventional model, and experimental data under oil film lubrication conditions: (a) vibration acceleration signals of the slider; (b) vibration acceleration signals at the middle position of the guide.

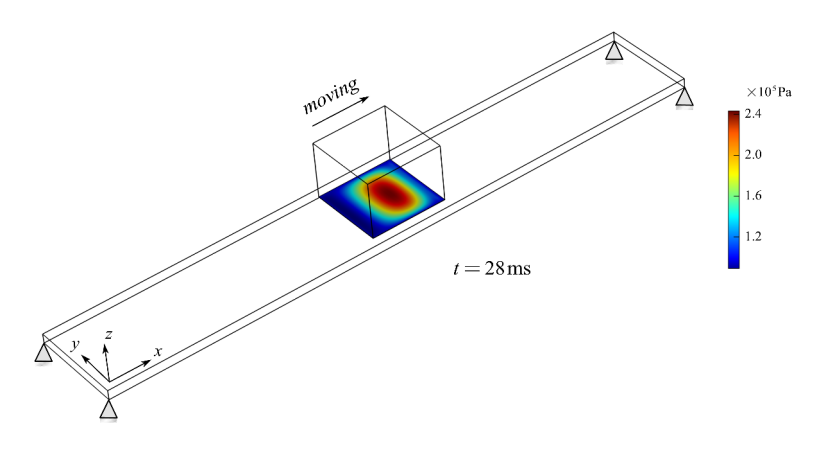


Fig. 8. Pressure distribution of oil film beneath the slider at 28 ms.

Data availability

The original codes and data used to support the findings of this study are available from the corresponding author upon request.

Received: 20 October 2024; Accepted: 28 January 2025

Published online: 11 March 2025

References

- 1. Shabana, A. A. Flexible Multibody Dynamics: Review of Past and Recent Developments. Multibody Syst Dyn 1, 189-222 (1997).
- 2. Tian, Q., Flores, P. & Lankarani, H. M. A comprehensive survey of the analytical, numerical and experimental methodologies for dynamics of multibody mechanical systems with clearance or imperfect joints. *Mech Mach Theory* 122, 1–57 (2018).
- 3. Skrinjar, L., Slavič, J. & Boltežar, M. A review of continuous contact-force models in multibody dynamics. *Int J Mech Sci* 145, 171–187 (2018).
- 4. Lei, Y., Adhikari, S. & Friswell, M. I. Vibration of nonlocal Kelvin-Voigt viscoelastic damped Timoshenko beams. *Int J Eng Sci* **66–67**, 1–13 (2013).
- 5. Schindeler, R. & Hashtrudi-Zaad, K. Online Identification of Environment Hunt-Crossley Models Using Polynomial Linearization. *IEEE Trans Robot* 34, 447–458 (2018).
- 6. Li, Y., Wang, C. & Huang, W. Dynamics analysis of planar rigid-flexible coupling deployable solar array system with multiple revolute clearance joints. *Mech Syst Signal Process* 117, 188–209 (2019).
- Ma, J. & Qian, L. Modeling and simulation of planar multibody systems considering multiple revolute clearance joints. Nonlinear Dyn 90, 1907–1940 (2017).
- 8. Zheng, X., Li, J., Wang, Q. & Liao, Q. A methodology for modeling and simulating frictional translational clearance joint in multibody systems including a flexible slider part. *Mech Mach Theory* **142**, 103603 (2019).
- 9. Guo, J. et al. A study on the effects of piston secondary motion in conjunction with clearance joints. *Mech Mach Theory* **149**, 103824 (2020)
- 10. Flores, P., Ambrósio, J., Claro, J. C. P., Lankarani, H. M. & Koshy, C. S. A study on dynamics of mechanical systems including joints with clearance and lubrication. *Mech Mach Theory* 41, 247–261 (2006).
- Chen, X., Gao, S. & Wang, T. Experimental verification of dynamic behavior for multi-link press mechanism with 2D revolute joint considering dry friction clearances and lubricated clearances. *Nonlinear Dyn* 109, 707–729 (2022).
- Cavalieri, F. J. & Cardona, A. Non-smooth model of a frictionless and dry three-dimensional revolute joint with clearance for multibody system dynamics. *Mech Mach Theory* 121, 335–354 (2018).
- Qian, M., Qin, Z., Yan, S. & Zhang, L. A comprehensive method for the contact detection of a translational clearance joint and dynamic response after its application in a crank-slider mechanism. *Mech Mach Theory* 145, 103717 (2020).
- Xing, M., Zhang, B., Deng, P., Xu, J. & Cui, Y. A comprehensive analysis of contact kinematics for planetary roller screw mechanism. Tribol Int 179, 108127 (2023).
- 15. Xing, M., Zhang, B., Deng, P., Xu, J. & Cui, Y. A novel wear prediction model for planetary roller screw based on universal sliding
- distance model. *Tribol Int* **175**, 107851 (2022).

 16. McMullen, R. M., Krygier, M. C., Torczynski, J. R. & Gallis, M. A. Navier-Stokes Equations Do Not Describe the Smallest Scales of
- Turbulence in Gases. *Phys Rev Lett* **128**, 114501 (2022).

 17. Rom, M. Physics-informed neural networks for the Reynolds equation with cavitation modeling. *Tribol Int* **179**, 108141 (2023).
- 18. Chen, X., Wang, T. & Jiang, S. Study on dynamic behavior of planar multibody system with multiple lubrication clearance joints. Eur J Mech ASolids 91, 104404 (2022).
- 19. Daniel, G. B., Machado, T. H. & Cavalca, K. L. Investigation on the influence of the cavitation boundaries on the dynamic behavior of planar mechanical systems with hydrodynamic bearings. *Mech Mach Theory* **99**, 19–36 (2016).
- Liu, S. et al. Modeling of lubricated translational joints in rigid-partially flexible multibody systems and its application in twostroke marine diesel engines. Tribol Int 165, 107244 (2022).
- 21. Liu, S. et al. Tribo-dynamic performances and vibration transmission of lubricated translational joints in marine engines. *Int J Mech Sci* 231, 107599 (2022).
- 22. Liu, S., Gao, L., Xing, M., Cui, Y. & Meng, X. A new 3-D multi-physics coupling model for lubricated piston-liner systems. *Int J Mech Sci* 272, 109194 (2024).
- 23. Ruggiero, A. & Sicilia, A. Lubrication modeling and wear calculation in artificial hip joint during the gait. *Tribol Int* **142**, 105993 (2020).
- 24. Gao, L. et al. A fully coupled tribo-dynamic model for piston-ring-liner system. Tribol Int 178, 107998 (2023).
- Gao, L. et al. A new method to establish coupled multi-physics model of lubricated pin-hole oscillating pair. Int J Mech Sci 264, 108818 (2024).
- Xing, M. et al. Elastohydrodynamic lubrication analysis with eccentric errors for planetary roller screw mechanism. Tribol Int 193, 109362 (2024).
- 27. Zhao, B., Dai, X.-D., Zhang, Z.-N. & Xie, Y.-B. A new numerical method for piston dynamics and lubrication analysis. *Tribol Int* **94**, 395–408 (2016).
- 28. Zhao, J., Sheng, W., Li, Z., Zhang, H. & Zhu, R. Effect of lubricant selection on the wear characteristics of spur gear under oil-air mixed lubrication. *Tribol Int* 167, 107382 (2022).
- Zhou, G., Qiao, J., Pu, W. & Zhong, P. Analysis of mixed lubrication performance of water-lubricated rubber tilting pad journal bearing. Tribol Int 169, 107423 (2022).
- Almeida, M., Bastos, F. & Vecchio, S. Fluid-Structure Interaction Analysis in Ball Bearings Subjected to Hydrodynamic and Mixed Lubrication. Appl Sci 13, 5660 (2023).
- 31. Salvaro D, Neves GO, Binder C, Klein AN, Biasoli de Mello JD. Influence of SiC polytypes on the mixed lubrication regime of self-lubricating composites containing in situ generated 2D turbostratic graphite. Tribol Int 2023;184:108446.
- 32. Chen, S., Guo, F., Wang, W. & Wang, Y. An improved mixed lubrication model for revealing the mechanism of high speed and frictional heat on sealing performance. *Tribol Int* 191, 109147 (2024).
- Chen, R. et al. Study on coupling transient mixed lubrication and time-varying wear of main bearing in actual operation of low-speed diesel engine. Tribol Int 191, 109159 (2024).
- 34. Stephan, S., Schmitt, S., Hasse, H. & Urbassek, H. M. Molecular dynamics simulation of the Stribeck curve: Boundary lubrication, mixed lubrication, and hydrodynamic lubrication on the atomistic level. *Friction* 11, 2342–2366 (2023).
- 35. Ali, M. K. A., Xianjun, H. & Jiang, H. Lubrication mechanism analysis of nickel-carbon-based tribological layer on sliding interfaces in automotive engines. *Tribol Int* **195**, 109595 (2024).
- 36. Yang, T. et al. Five-DOF nonlinear tribo-dynamic analysis for coupled bearings during start-up. Int J Mech Sci 269, 109068 (2024).
- 37. Liao, G., Wang, W., Wang, B., Chen, Q. & Liu, X. Transient mixed-lubrication and contact behavior analysis of metal liquid film under magneto-thermal effect. *Int J Mech Sci* 271, 109142 (2024).
- 38. Xie, Z., Zhang, H., Zhao, B., Du, P. & Zhang, X. Effect of turbulence on lubrication behaviors of a new bearing under bi-misaligned status: Theoretical and experimental study. *Mech Syst Signal Process* 218, 111547 (2024).
- 39. Xie, Z., Jiao, J., Zhao, B., Zhang, J. & Xu, F. Theoretical and experimental research on the effect of bi-directional misalignment on the static and dynamic characteristics of a novel bearing. *Mech Syst Signal Process* 208, 111041 (2024).
- 40. Dlugoš, J. & Novotný, P. Effective Implementation of Elastohydrodynamic Lubrication of Rough Surfaces into Multibody Dynamics Software. *Appl Sci* 11, 1488 (2021).
- 41. Zhao, J., Li, Y., Xie, L. & Liu, J. Lubrication failure analysis of camshaft bearings in V6 diesel engine. *Eng Fail Anal* **150**, 107329 (2023).
- 42. Bifeng, Y., Jiajun, Z., Bo, X., Gongyin, H. & Manying, Y. Friction and Wear Performance of Double-bump Design of Piston Skirt Main Thrust Side. Int J Automot Technol 21, 1579–1586 (2020).

| https://doi.org/10.1038/s41598-025-88240-9

Scientific Reports |

- 43. Li, Y. et al. Development of a reverse-loop scavenged poppet-valve 2-stroke diesel engine for down speed and performance comparisons with its 4-stroke baseline. *Fuel* 322, 124199 (2022).
- Shabana, A. A. An overview of the ANCF approach, justifications for its use, implementation issues, and future research directions. Multibody Syst Dyn 58, 433–477 (2023).
- 45. Gantoi FM, Brown MA, Shabana AA. ANCF Finite Element/Multibody System Formulation of the Ligament/Bone Insertion Site Constraints. J Comput Nonlinear Dyn 2010;5.
- Tian, Q. et al. Coupling dynamics of a geared multibody system supported by ElastoHydroDynamic lubricated cylindrical joints. Multibody Syst Dyn 33, 259–284 (2015).
- 47. Li, Y., Yang, Y., Li, M., Liu, Y. & Huang, Y. Dynamics analysis and wear prediction of rigid-flexible coupling deployable solar array system with clearance joints considering solid lubrication. *Mech Syst Signal Process* 162, 108059 (2022).
- 48. Westin, C. & Irani, R. A. Efficient semi-implicit numerical integration of ANCF and ALE-ANCF cable models with holonomic constraints. *Comput Mech* 71, 789–800 (2023).
- 49. Fan, B. & Wang, Z. Vibration analysis of radial tire using the 3D rotating hyperelastic composite REF based on ANCF. Appl Math Model 126, 206–231 (2024).
- 50. Liu, D., Ai, S., Sun, L., Wei, J. & He, N. Numerical modelling of offshore risers conveying slug flow under the ALE-ANCF framework. *Ocean Eng* 235, 109415 (2021).
- 51. Taylor, M., Serban, R. & Negrut, D. Implementation implications on the performance of ANCF simulations. *Int J Non-Linear Mech* 149, 104328 (2023).
- 52. Grossi, E. & Shabana, A. A. Analysis of high-frequency ANCF modes: Navier-Stokes physical damping and implicit numerical integration. *Acta Mech* 230, 2581–2605 (2019).
- 53. Fan, B., Wang, Z. & Wang, Q. Nonlinear forced transient response of rotating ring on the elastic foundation by using adaptive ANCF curved beam element. *Appl Math Model* **108**, 748–769 (2022).
- Liao, K., Duan, W., Ma, Q., Ma, S. & Yang, J. Numerical Simulation of Green Water on Deck with a Hybrid Eulerian-Lagrangian Method. J Ship Res 66, 73–90 (2022).
- Udaykumar, H. S., Shyy, W. & Rao, M. M. Elafint: A Mixed Eulerian-Lagrangian Method for Fluid Flows with Complex and Moving Boundaries. Int J Numer Methods Fluids 22, 691–712 (1996).
- 56. Patir, N. & Cheng, H. S. An Average Flow Model for Determining Effects of Three-Dimensional Roughness on Partial Hydrodynamic Lubrication. *J Lubr Technol* **100**, 12–17 (1978).
- 57. Patir, N. & Cheng, H. S. Application of Average Flow Model to Lubrication Between Rough Sliding Surfaces. *J Lubr Technol* 101, 220–229 (1979).
- 58. Wu, C. & Zheng, L. An Average Reynolds Equation for Partial Film Lubrication With a Contact Factor. J Tribol 111, 188–191 (1989).
- 59. Greenwood, J. A. & Tripp, J. H. The Contact of Two Nominally Flat Rough Surfaces. Proc Inst Mech Eng 185, 625-633 (1970).
- 60. Dan, S., Tarafder, P. & Ghosh, S. Adaptive wavelet-enhanced cohesive zone phase-field FE model for crack evolution in piezoelectric composites. *Comput Methods Appl Mech Eng* **392**, 114636 (2022).
- 61. Bürger, L. & Naets, F. High fidelity nonlinear finite element tire modeling for dynamic analysis: Total Lagrangian formulation in rolling contact. *J Sound Vib* **571**, 118098 (2024).
- Busto, S., Dumbser, M. & Río-Martín, L. An Arbitrary-Lagrangian-Eulerian hybrid finite volume/finite element method on moving unstructured meshes for the Navier-Stokes equations. Appl Math Comput 437, 127539 (2023).
- 63. Malinarič, S. The Application of the Finite Elements Method in the Transient Measurements of Thermophysical Parameters. Int J Thermophys 45, 22 (2024).
- 64. Čertík Ó, Pask JE, Fernando I, Goswami R, Sukumar N, Collins LeeA, et al. High-order finite element method for atomic structure calculations. Comput Phys Commun 2024;297:109051.
- 65. Sun, T., Wang, P., Zhang, G. & Chai, Y. Transient analyses of wave propagations in nonhomogeneous media employing the novel finite element method with the appropriate enrichment function. *Comput Math Appl* 129, 90–112 (2023).
- 66. de Prenter, F., Verhoosel, C. V., van Brummelen, E. H., Larson, M. G. & Badia, S. Stability and Conditioning of Immersed Finite Element Methods: Analysis and Remedies. *Arch Comput Methods Eng* 30, 3617–3656 (2023).
- 67. Qin, Q., Song, L. & Wang, Q. High-order meshless method based on the generalized finite difference method for 2D and 3D elliptic interface problems. *Appl Math Lett* 137, 108479 (2023).
- 68. Ju, B. & Qu, W. Three-dimensional application of the meshless generalized finite difference method for solving the extended Fisher-Kolmogorov equation. *Appl Math Lett* **136**, 108458 (2023).
- 69. Pasha, S. A., Nawaz, Y. & Arif, M. S. On the nonstandard finite difference method for reaction-diffusion models. *Chaos Solitons Fractals* **166**, 112929 (2023).
- 70. Zhou, H., Hu, K., Mao, L., Sun, M. & Cao, J. Research on planing motion and stability of amphibious aircraft in waves based on
- cartesian grid finite difference method. *Ocean Eng* 272, 113848 (2023).
 Zhao, J., Jiang, X. & Xu, Y. A kind of generalized backward differentiation formulae for solving fractional differential equations. *Appl Math Comput* 419, 126872 (2022).
- 72. Li, R., Meng, X., Dong, J. & Li, W. Transient tribo-dynamic analysis of crosshead slipper in low-speed marine diesel engines during engine startup. *Friction* 9, 1504–1527 (2021).
- 73. Li, R., Meng, X. & Xie, Y. A new coupling tribodynamic model of crosshead slipper-guide system and piston skirt-liner system of low-speed marine diesel engines. *Tribol Int* 117, 189–205 (2018).
- 74. Pourzeynali, S., Zhu, X., Ghari Zadeh, A., Rashidi, M. & Samali, B. Comprehensive Study of Moving Load Identification on Bridge Structures Using the Explicit Form of Newmark-β Method: Numerical and Experimental Studies. *Remote Sens* 13, 2291 (2021).
- Wang, J. et al. Dynamic analysis of magnetorheological damper incorporating elastic ring in coupled multi-physical fields. Mech Syst Signal Process 208, 111040 (2024).
- 76. Jiang, J., Cui, W., Chen, S., Guo, X. & Zhao, J. A novel dynamic load identification method based on improved basis functions and implicit Newmark-β for continuous system with unknown initial conditions. *Mech Syst Signal Process* **208**, 110987 (2024).
- 77. Negrut, D., Rampalli, R., Ottarsson, G. & Sajdak, A. On an Implementation of the Hilber-Hughes-Taylor Method in the Context of Index 3 Differential-Algebraic Equations of Multibody Dynamics (DETC2005-85096). *J Comput Nonlinear Dyn* 2, 73–85 (2006).
- 78. Chung, J. & Hulbert, G. M. A Time Integration Algorithm for Structural Dynamics With Improved Numerical Dissipation: The Generalized-α Method. *J Appl Mech* **60**, 371–375 (1993).
- Liu, B. A Nitsche stabilized finite element method: Application for heat and mass transfer and fluid-structure interaction. Comput Methods Appl Mech Eng 386, 114101 (2021).
- Jansen, K. E., Whiting, C. H. & Hulbert, G. M. A generalized-α method for integrating the filtered Navier-Stokes equations with a stabilized finite element method. Comput Methods Appl Mech Eng 190, 305–319 (2000).
- 81. Behnoudfar, P., Loli, G., Reali, A., Sangalli, G. & Calo, V. M. Explicit high-order generalized- α methods for isogeometric analysis of structural dynamics. *Comput Methods Appl Mech Eng* **389**, 114344 (2022).
- 82. Gobat, J. I. & Grosenbaugh, M. A. Application of the generalized-α method to the time integration of the cable dynamics equations. *Comput Methods Appl Mech Eng* **190**, 4817–4829 (2001).
- 83. Chen, Y., Li, Y., Huang, Y., Li, M. & Liu, Y. An efficient algorithm based on Broyden's and generalized-α method for large scale flexible multi-body systems. *Appl Math Model* **106**, 742–755 (2022).

Acknowledgements

This study is sponsored by the National Natural Science Foundation of China (Grant No. 52305121 and 52171315), the Postdoctoral Fellowship Program of CPSF (Grant No. GZC20231582), the National Key Laboratory of Marine Engine Science and Technology, and the project of the Key Technology for High Reliability Design and Verification of Marine Engines.

Author contributions

Shuo Liu and Yi Cui wrote the main manuscript text. Shuo Liu, Mingcai Xing, and Lining Gao performed the experiments. Feng Zhu proofread the grammer. All authors reviewed the manuscript.

Declarations

Competing interests

The authors declare no competing interests.

Additional information

Correspondence and requests for materials should be addressed to Y.C.

Reprints and permissions information is available at www.nature.com/reprints.

Publisher's note Springer Nature remains neutral with regard to jurisdictional claims in published maps and institutional affiliations.

Open Access This article is licensed under a Creative Commons Attribution-NonCommercial-NoDerivatives 4.0 International License, which permits any non-commercial use, sharing, distribution and reproduction in any medium or format, as long as you give appropriate credit to the original author(s) and the source, provide a link to the Creative Commons licence, and indicate if you modified the licensed material. You do not have permission under this licence to share adapted material derived from this article or parts of it. The images or other third party material in this article are included in the article's Creative Commons licence, unless indicated otherwise in a credit line to the material. If material is not included in the article's Creative Commons licence and your intended use is not permitted by statutory regulation or exceeds the permitted use, you will need to obtain permission directly from the copyright holder. To view a copy of this licence, visit https://creativecommons.org/licenses/by-nc-nd/4.0/.

© The Author(s) 2025